TALLINN UNIVERSITY OF TECHNOLOGY

Faculty of Science

Chair of Oceanography

ESTIMATION OF WAVE FIELD PARAMETERS FROM SAR IMAGERY IN THE BALTIC SEA

Master's thesis

Sander Rikka

Supervisor: PhD Rivo Uiboupin

Marine System Institute at Tallinn University of Technology

Earth Sciences

2014

Declaration

Hereby I declare that this master thesis, my original investigation and achievement, submitted for the master degree at Tallinn University of Technology has not been submitted for any academic degree. All content and ideas drawn directly or indirectly from external sources are indicated as such.

Sander Rikka

(Signature and date)

Supervisor: *Rivo Uiboupin*

Work meets the requirements for master's thesis.

(Signature and date)

The defence chief:

Accepted for defence of a thesis

……

(Name, signature, date)

TALLINNA TEHNIKAÜLIKOOL

Matemaatika-loodusteaduskond

Okeanograafia õppetool

LAINEPARAMEETRITE MÄÄRAMINE LÄÄNEMERES SAR SENSORI ANDMETE PÕHJAL

Magistritöö

Sander Rikka

Juhendaja: PhD Rivo Uiboupin

Meresüsteemide instituut

Maateadused

2014

Table of contents

1 INTRODUCTION

The Baltic Sea has offered a great amount of research material to the scientists who focus on the wind waves. Since the complexity of the Baltic Sea, mainly shallow areas, its narrow bays, with thousands of islands, very complex wave conditions are produced. In addition, heavy ice conditions during winter complicate both visual and instrumental measurements.

Systematical wave measurements began in the early 1970s by the Helsinki University of Technology and the Finnish Institute of Marine Research (FIMR). Periodical measurements started in the Bothnian Sea from 1972 (Kahma, 1976; Kahma, 1981). Since floating devices are usually removed before ice season (Kahma, et al., 2003), model estimations become important.

Previously, many studies have been carried out over Baltic Sea waves by many authors, for example Alari (2013), Räämet (2010), or Soomere et al. (2008). Mainly two different wave models have been used in Baltic Sea wave studies – SWAN (Simulating WAves Nearshore) and WAM (WAve Model). SWAN is a third-generation wave model for obtaining realistic estimates of wave parameters in coastal areas, lakes and estuaries from given wind, bottom and current conditions (SWAN team, 2014). WAM wave model is likely to be the most used and well tested wave model in the world (The WAMDI Group, 1988). Although, intial WAM model was built to estimate open ocean waves (Komen, et al., 1994), it is now used by many meteorological institutes around the Baltic Sea, including Finnish Meteorological Institute (FMI), Danish Meteorological Institute (DMI), etc.

Since 2007, when TerraSAR-X (TSX) reached its orbit, new opportunities have disclosed for retrieval of information about surface wind waves in the Baltic Sea. Its high resolution data (0.75 – 1.5 m per pixel) compared to other sensors (e.g. ENVISAT/ASAR), enables to detect two dimensional (2D) wave spectrums even in

the Baltic Sea where the scale of waves is significantly smaller than those in the ocean.

Previously, it is demonstrated by many authors (Li, et al., 2010; Diaz Méndez, et al., 2010; Lehner, et al., 2012; Bruck & Lehner, 2013), that obtaining wave field parameters from SAR imagery is relatively straightforward. These studies were carried out over the regions where ocean swell waves play a major part of occurring sea state. However, in the Baltic Sea the sea state is mostly affected by the geometry and by the local wind regime together with the fetch limitation. Since TSX sensor is capable to detect wavelengths that are longer than 30 m (Lehner, et al., 2012) it could be suitable for Baltic Sea conditions.

Although, previously mentioned studies also concentrate on significant wave height which is an important parameter from navigatoin point of view, the current study does not include wave height analysis from SAR imagery. The SAR images provide a good opportunity to investigate distribution of wavelengths in the Baltic Sea. As higher wind speeds produce very structural wave fields, it is possible to obtain dominant wavenumber and thus dominant wavelengths using Fast Fourier Transform.

The study is concentrated on the wave fields of the Gulf of Finland (GoF), Northern Baltic Proper (NBP) and the Gulf of Riga (GoR). The results from 2D image spectra - dominant wavelength, wave propagation direction and peak period - are compared with *in situ* measurements and the hindcast results from SWAN wave model. The capabilities of TSX are also found out via the analysis.

The specific objectives of this work are:

- Investigation of high-resolution X-band SAR sensor capabilities to estimate wave field parameters in the Baltic Sea
- Development of method for retrieving wave field parameters
- Validation of the wave field parameters retrieved from 2D image spectra against *in situ* measurements data and wave model outputs
- Investigation of surface wind waves through the analysis of SAR sensor images

- Demonstration of advantages of wave fields calculation from TSX imagery: case studies
- Investigation of complex wave field cases with images over open ocean (long swell waves interact with the short wind waves) using developed algorithm

2 BALTIC SEA

The Baltic Sea is a large inland sea with seasonal ice-coverage located between 53° N to 66° N latitude and from 9° E to 30° E longitude. The total area of the Baltic sea with its several topographically and geographically separated sub-basins is 392,978 km^2 (Figure 1). The mean water depth is 54 m whereas the deepest part, Landsort Deep, reaches 459 m (Leppäranta & Myrberg, 2009).

The study concentrates on GoR, GoF and NBP and main wave characteristics of these locations are given below. The longest possible distance where waves can grow in the Baltic Sea is 700 km in the Baltic Proper (BP&NBP; Figure 1). Along the major axis of the Gulf of Finland (GoF; Figure 1) the longest fetch is 500 km and in the Gulf of Riga (GoR; Figure 1) it is 150 km.

2.1 Wave distribution in the Baltic Sea

Since 1970s, instrumental wave measurements have been carried out in the Baltic Sea region, while before, only visual observations were available (Tuomi, et al., 2011). In the Baltic Sea, the dominant wavelengths are between 20 – 70 m. Depending on wind speed, duration, direction stability and water depth, wavelengths can grow up to 130 m (Kriaučiūnienė, et al., 2006).

The waves are propagating in the direction of the wind as the dominant wind direction for the Baltic Sea region is from sector 180 – 270° (Jaagus & Kull, 2011). However, together with the geometry of the Baltic Sea, slanting fetch cases are often observed where the wind direction and peak wave direction differ from each other up to 50° in deep water. This phenomenon is well documented for the GoF (Petterson, et al., 2010), whereas other sub-basins have also fetch restrictions in the upwind direction.

Wave periods remain short, usually not exceeding 7 – 8 s which means that long-period swell is almost absent (Leppäranta & Myrberg, 2009).

The study area was selected to be the Northern Baltic Proper, Gulf of Finland and the Gulf of Riga. Images were also acquired over the open part of the Baltic Sea (Figure 1) and over the west coast of Saaremaa and Hiiumaa. The main wave characteristics of these locations are given out in the following paragraphs.

Surface wave statistics for the GoF based on wave buoy measurements in 1982 – 1985 are given in Kahma and Petterson (1993). The observation site, nearly in the middle of the GoF at 59° 58.5′ N, 25° 14.0′ E, near Kalbådagrund, has bottom depth of about 60 m. Wave conditions were characterized by mean significant wave height which was between 0.5 m in spring and 1.3 m in winter. Wave peak periods were 3.8 – 5.5 s correspondingly. Stormy conditions can produce higher waves in GoF. For example, Soomere et al. (2008) analyzed the wave conditions of the windstorm Gudrun, from 7 January to 13 January 2005. During the storm, significant wave height exceeded 4 m and remained about 4 m many hours in the site located north-westwards from the Island of Naissaar (59°37.1′N, 24°29.1′E). The observed wave peak periods exceeded 8 s during a large part of the storm and reached even 12 s. The all-time record value of instrumentally measured significant wave height in the GoF is 5.2 m (Tuomi, et al., 2011).

There are relatively low wave heights in the GoR compared to GoF. According to Suursaar et al. (2012), the annual mean wave heights were between 0.25 m to nearly 0.5 m. During their measurements at northern part of the GoR, significant wave height reached 2 m. Yet again, stormy conditions produce much more violent sea state. Alari, V. and Kõuts, T. (2012) analyzed in their work previously mentioned windstorm Gudrun. High surge in the Pärnu bay caused very high significant wave height values in the shallow areas, damaging coastal areas. Modelled values of significant wave height reached 3 m at the entrance of the bay and were even higher at the open areas. The measured peak period for the waves of GoR fluctuate between 2.3 – 8 s (Raudsepp, et al., 2011).

NBP is one of the locations where very high waves are observed. According to Tuomi et al. (2011), the highest measured significant wave height is 8.2 meters. By looking at the results given by the operational wave models, wave height values can grow even higher (Soomere, et al., 2008). During stormy seas, wave peak period is also longest in open parts of the Baltic Sea. During the windstorm Gudrun, wave peak period exceeded 10 s for nearly 24 h and reached highest value of 12 s (Soomere, et al. 2008). It is due to ice coverage, that the instrumental measurements at the northern part of the Baltic Sea are not continuous.

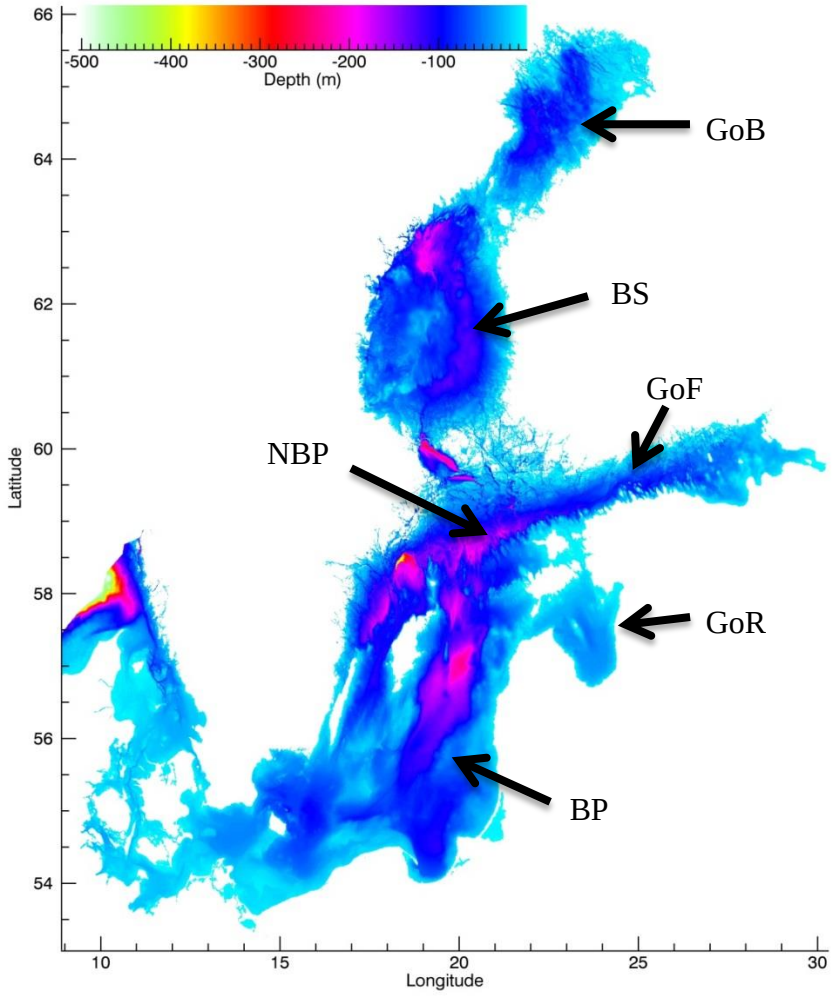

Figure 1. Bathymetry of the Baltic Sea (Baltic Sea Hydrographic Commission, 2013). BP – Baltic Proper; BS – Botnia Sea; GoB – Gulf of Botnia; GoF – Gulf of Finland; GoR – Gulf of Riga; NBP – Northern Baltic Proper.

3 SYNTHETIC APERTURE RADAR

Synthetic Aperture Radar (SAR) sensor (Figure 2) has an unique capability to provide two-dimensional information about sea surface. SAR sensors have daylight and weather independency and together with global high resolution coverage, these sensors are particularly suitable for many ocean and coastal applications (Lehner, et al., 2008).

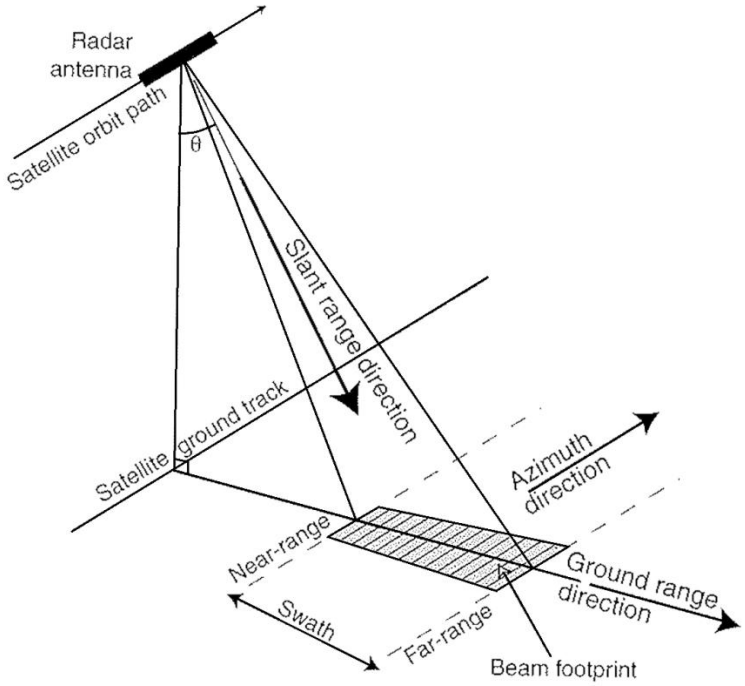

Figure 2. Schematic overview of SAR geometry.

Since radars generate their own microwave energy flux, the polarization conditions of the transmitted pulses is known. Generally, antenna on satellite radars are used to produce plane polarized waves. For plane polarized radiation, the direction of the polarization is important in relation to reflection or transmission at the surface. An oblique viewing radar generally maintains its orientation relative to the mean sea surface and so it is designed to be able to generate purely *H*-polarized

or purely *V*-polarized microwave pulses. The backscattered radiation will contain all orientations of polarization, in consequence it is possible to measure separately different echoes from sea surface. Hence the four distinct echoes, *HH*, *HV*, *VH*, *VV*, can be detected. These correspond respectively to, receive *H*-polarized energy from transmitted *H*-polarized beam, receive *V*-polarized energy from *H*-polarized beam, and so on.

3.1 Overview of TerraSAR-X satellite

The TSX satellite, operated by German Aerospace Center (DLR), was launched in June 2007. It is designed to orbit the Earth sun-synchronously at the nominal height of 514.8 km. It operates with wavelength of 31 mm and a frequency of 9.65 GHz. Its inclination is 97.44° with respect to the Earth's equator hence its revisit cycle is 11 days. Yet the same region can be imaged by different incidence angles after 3 days dependent on scene latitude. Incidence angles range between 20° to 60°. Additional information about TSX sensor, basic products and data structure can be found in Eineder et al (2008). Since January 2008, data and different products have been available for researchers and commercial customers.

TSX operates in four different modes. The technical parameters of the modes are brought out in Table 1. SAR images are used for wide variety of applications. For example, SAR data is commonly used for ship-, ice- and oil-slick-detection. Detecting underwater topography fields is analyzed by Brusch et al (2011). Not to mention that SAR is often used for measurements of wind fields, it also has many applications over land areas. For instance, X-band SAR sensor usability for flood mapping in temperate forest is analyzed by Voormansik (2014).

Table 1. Basic imaging modes of TerraSAR-X.[1]

Imaging modes				
	ScanSAR	StripMap	SpotLight	HR[2] SpotLight
Swath width (km)	100	30	10	10
Product length (km)	150	50	10	5
Incidence angle (°)	20-45	20-55	20-55	20-55
Azimuth resolution (m)	18.5	3.3	1.7	1.1
Range resolution (m)	1.7-3.5	1.7-3.5	1.5-3.5	1.5-3.5
Polarizations	HH or VV	HH or VV	HH or VV	HH or VV

3.2 Detecting wave fields from radar imagery

SAR sensor measures the backscatter which is a measure of the roughness of the surface. The simplified scheme of backscattering from surface is given in Figure 3. The flat calm surface (Figure 3a)) will reflect energy away from it by following the normal laws of light reflection. In slightly rougher surface (Figure 3b)) some energy is reflected back to the radar because of the small amount of diffuse scattering. In Figure 3c) the surface is very rough and the diffuse scattering ensures that radar receives a strong return.

Over the water surface, short surface waves, whose wavelength is similar to the ones of the radar signal, are the cause of surface roughness. Constructive interference in the direction of sensor occurs, when these small capillary waves (Bragg waves) with wavelength λ_B (Figure 4) are related to radar wave frequency or wavelength λ_r at the incidence angle θ_i by the following equation:

$$\lambda_B = \lambda_r / 2 sin\theta_i. \quad (1)$$

For moderate incidence angles (20° – 60°), Bragg scattering is the dominant scattering mechanism (Lehner, et al., 1998). The above mentioned Bragg condition is

[1] Table is given for single polarization image acquisition
[2] HR – High-Resolution

nearly always satisfied because of the uniform distribution of the small-scale waves (Jackson & Koch, 2005).

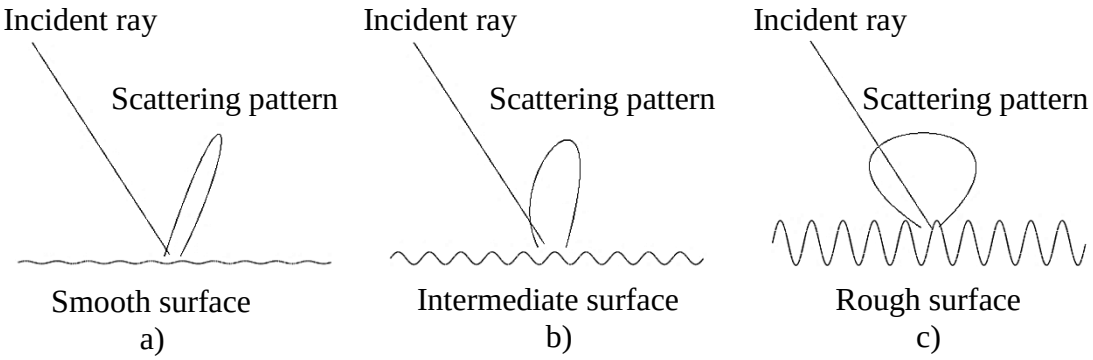

Figure 3. The directional envelope of microwave scattering from a) a calm surface, b) a roughened surface, c) a rough surface.

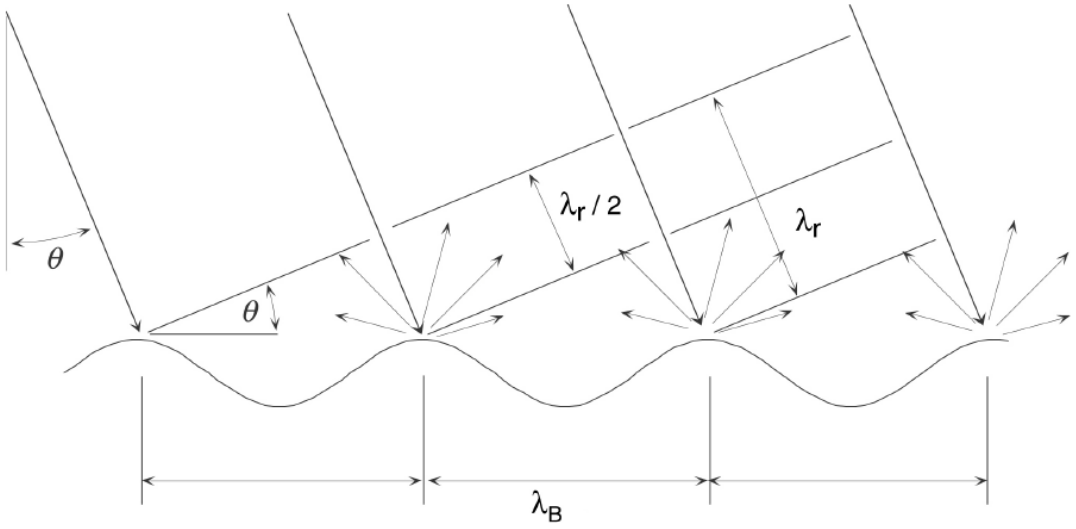

Figure 4. Illustration of Bragg scattering, λ_r is the radar wavelength, λ_B sea surface wavelength and θ_i is local incidence angle.

Two-scale approximation is used to describe the imaging process of long ocean waves by SAR as short Bragg waves are modulated by the long ocean gravity waves. There are three possible mechanisms in which long waves modify Bragg waves, hence effecting SAR imaging: the tilt, hydrodynamic and velocity bunching modulation (Jackson & Koch, 2005).

3.2.1 Mechanism 1: tilt modulation

The principal of tilt modulation is illustrated on Figure 5. Varying slope of the gravity waves changes the local incidence angle θ_i and therefore the Bragg scattering. These tilting waves act as reflecting mirrors to the incoming radar waves, thus the backscatter increases as the incidence angle increases. It must be mentioned that this mechanism applies only to the range-travelling waves (Jackson & Koch, 2005).

3.2.2 Mechanism 2: hydrodynamic modulation

Hydrodynamic modulation is caused by the water particles within the gravity wave. These particles near the surface have a circular path as the wave passes. Therefore, patterns of horizontal convergence of capillary waves on the crest and a divergence in the troughs are observed (Figure 5). This leads to the radar backscatter which generates patterns of light and dark on the SAR image. Again, this mechanism is strongest on the waves that are propagating in the range direction, or have a significant component of their motion in the range direction. Both mechanisms, tilt and hydrodynamic modulation, are stronger at horizontal polarizations than vertical (Jackson & Koch, 2005).

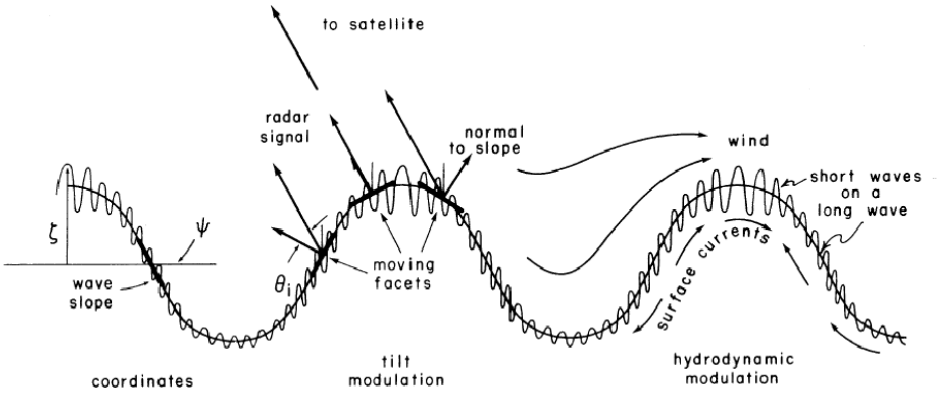

Figure 5. Illustration of two mechanisms: tilt and hydrodynamic modulation.

3.2.3 Mechanism 3: velocity bunching modulation

The third modulation applies on the waves propagating in the azimuthal direction. If a target has a velocity component, an additional velocity component (Doppler shift) is produced due to the wave's orbital motion. The radar interprets this as a position shift in the azimuth direction. Because of the periodic orbital motion of the long wave, an apparent increase (bunching) and decrease in the density of scatters occurs which makes azimuth-traveling waves detectable for SAR sensor although they are shifted from their original position (Jackson & Koch, 2005).

As waves are moving during image acquisition, some artefacts are caused. This phenomenon is seen for azimuth-travelling waves. Those waves that are shorter than a certain threshold value are not imaged by the SAR. This limitation is called azimuth cut-off wavelength. There is a relatively simple empirical relationship for cut-off wavelength λ_{min}, expressed by the equation (Beal, et al., 1983):

$$\lambda_{min} = \frac{R_0}{V_{SAR}} \sqrt{H_{sig}} \tag{2}$$

where R_0 is the slant range, V_{SAR} is the platform velocity and H_{sig} is significant wave height.

3.3 Usage of Fourier Transform to retrieve wave parameters

The most common way to represent pixel location in the image processing is the spatial domain by column, row and value as x, y and z respectively. Yet sometimes it may be too inefficient and different domain is required to offer compression benefits. Therefore the Fast Fourier Transform (FFT) is used for transform spatial domain into frequency. The frequency domain is the basis for many image filters used to remove noise, sharpen an image, analyze repeating patterns or extract features. In the frequency domain, pixel location is represented by its x- and y-frequencies and its value is represented by amplitude.

The FFT is commonly used for many applications in engineering, science and mathematics because it is significantly faster than Direct Fourier Transform (DFT;

Equation 3). For example, computing the DFT of N points takes O(N^2) operations by the definition whereas FFT can manage the same data amount with O(N log N) operations.

$$F(u) = \frac{1}{N}\sum_{x=0}^{N-1} f(x) e^{\frac{-j2\pi ux}{N}} \tag{3}$$

By applying the FFT for SAR subimage, a two-dimensional (2D) image spectrum is retrieved. The maximum values on the spectrum indicate the peak wavenumber and peak propagation direction of all visible waves on the subimage. Refracting waves around island for example produce spectrums with several peaks. Since peak wavenumber is directly obtained from the spectrum, wavelength is easily calculated by taking reciprocal value:

$$L = \frac{2\pi}{\sqrt{k_x^2 + k_y^2}} \tag{4}$$

and peak wave propagation direction is calculated by:

$$\gamma = \arctan\left(\frac{k_y}{k_x}\right) \tag{5}$$

where L is the peak wavelength and γ is the peak direction with respect to the image spectrum. Peak coordinates in the wave number space is given with k_x and k_y. Due to static nature of SAR image, the retrieved peak direction have an ambiguity of 180° which have to be eliminated with the information about wave direction from the cross spectrum or other sources.

Surface waves are described by the dispersion relationship, which relates angular frequency ω to wavenumber k and water depth h:

$$\omega = \sqrt{gk \tanh(kh)} \tag{6}$$

where g is acceleration of gravity and *tanh* denotes as hyperbolic tangent. In deep water, where $kh \to \infty$, the hyperbolic tangent *tanh(kh)* equals nearly one and eq. (6) reduces to $\omega = \sqrt{gk}$. Simple translation of angular frequency $\omega = 2\pi/T$, where T is referred as period, allows to link periods from different sources, SAR and wave measurements or wave model outputs.

4 DATA

4.1 Overview of SAR data

For the current work, the TSX multilook ground range detect (MGD) Stripmap products were used. Images were acquired with both HH and VV polarizations. Single image usually covers the area of about 30 x 50 km with pixel spacing 1.25 m. The azimuth resolution of the image is 3.3 m, range resolution, depending on the incidence angle of the acquisition, varies between 1.7 – 3.5 m (Table 1).

A total of 43 TSX images were acquired between 2012 and 2013 over the GoF, GoR and NBP (Table 2). Images were acquired during stormy conditions (wind speed over 9 m/s) for better wave field. The borderlines of the acquired images (pink polygons) can be seen in the Figure 6.

In order to emphasize the difference between waves in the Baltic Sea and in open ocean, eight images were acquired from various locations around the world (Table 3). Another purpose of using the open ocean images was to analyze complex wave fields (wave spectrum with multiple peaks) and to estimate the performance of developed algorithm in different conditions, i.e. to analyze classical case on the ocean when long swell waves interact with the short wind waves.

All the satellite images are acquired via the DLR's Earth Observation webpage (EOWEB). Images over the Baltic Sea region were future acquisitions, global images, ordered by other users, were downloaded from EOWEB catalogue.

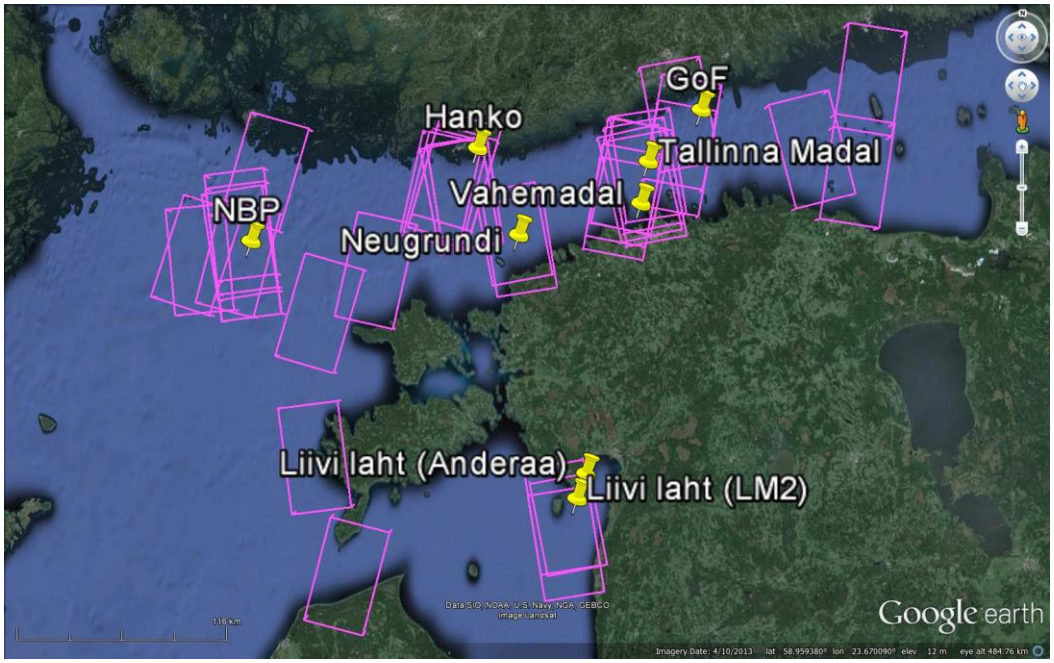

Figure 6. Borderlines of TSX images (pink polygons) and buoy locations (yellow pinheads).

4.2 Description of buoy data

Extracted wave field parameters from SAR data were compared with *in situ* buoy measurements (Figure 6). Three different buoy types were used in the Baltic Sea: ADCP (Acoustic Doppler Current Profiler), waveriders and pressure sensors. ADCP was, located on the seafloor near Hanko peninsula, has the same working principal, as SAR sensor but uses acoustic wave instead of electromagnetic. Significant wave height, peak period and average direction were retrieved from the dataset. Waverider buoy has an unique capability to measure wave density spectrum allowing the comparison with image wavenumber spectrum of the propagation direction (Figure 7c)). NBP, GoF and small period of time in Tallinna Madal station measurements are made by this type of buoy. Other station measurements were made by pressure sensor which allows comparing wave height and period. Overview of buoy characteristics can be seen in Table 2.

For the images over open ocean, the state of wave field is also needed. Measured spectral wave density information was downloaded via National Data Buoy Center

(NDBC) webpage. All other wave field parameters (peak direction and peak period) were also downloaded via the website. Overview of buoy data can be seen in Table 3.

4.3 SWAN wave model data

The SAR based wave field parameters were compared with numerical wave model data provided by Marine System Institute (MSI) at Tallinn University of Technology (TUT) is used. The wave model used is third generation wave model SWAN (SWAN team, 2014) which uses two-dimensional wave action density spectrum to describe waves. In SWAN, the time dependent wave action equation consists of four terms: the local rate of change of action density, the propagation of wave energy in two dimensional geographical spaces, the effect of shifting of the radian frequency due to variations in depth and mean currents, and the depth-induced and current-induced refraction. The equation understandably contains all physical processes known that generate, dissipate or redistribute wave energy.

The data extracted from SWAN wave model were significant wave height, peak wave period, peak wave direction and peak wavelength. SWAN is running operationally and covers the Baltic Sea with one nautical mile grid. Recalculations are made twice per day using ECMWF[3] forcing.

[3] European Centre for Medium-Range Weather Forecasts

Table 2. Overview of buoy characteristics and match-up pairs with satellite images in both polarizations.

Name	Longitude	Latitude	Measurement period	Data origin	Sensor type	Depth (m)	Match-up, HH pol.	Match-up, VV pol.
NBP	21° 00' E	59° 15' N	Ice-free seasons	FMI[4]	Waverider	90	3	3
GoF	25° 14' E	59° 58' N	Ice-free seasons	FMI	Waverider	60	1	2
Hanko	23° 06'07" E	59° 45'3" N	8.09 - 26.11.2013	Luode[5]	ADCP	19	2	5
Tallinna Madal	24° 43'890' E	59° 42'723" N	All seasons	MSI	Pressure	17	7	5
Tallinna Madal	24° 43'30" E	59° 42'10" N	11.10 - 17.11.2013	MSI	Waverider	17	1	2
Vahemadal	24° 39'973" E	59° 30'613" N	All seasons	MSI	Pressure	7.5	5	3
Liivi_1	24° 07'528" E	58° 05'161" N	25.08 - 17.09.2012	MSI	Pressure	15	2	-
Liivi_2	24° 11'063" E	58° 06'387" N	25.08 - 21.09.2012	MSI	Pressure	13	3	-
Neugrundi	23° 31'332" E	59° 20'824" N	11.09 - 25.09.2012	MSI	Pressure	17	2	-
						Total	**25**	**18**

[4] Finnish Meteorological Institute, www.fmi.fi
[5] Luode Consulting Oy, www.luode.net

Table 3. Overview of global buoy characteristics and match-up pairs with satellite images.

Buoy flag	Longitude	Latitude	Location	Data origin	Sensor type	Depth (m)	Date	SAR image polarization
51100	153° 54'0'' W	23° 33'30'' N	Northern Hawaii	NDBC	AMPS[6]	4754	26.02.2012	VV
51004	152° 22'55'' W	17° 31'31''N	Southeast Hawaii	NDBC	AMPS	5082	28.04.2012	VV
42012	87° 33'19'' W	30° 3'55'' N	Gulf of Mexico	NDBC	ARES 4.4[7]	28	11.07.2012	VV
46076	147° 58'59'' W	59° 29'54'' N	Gulf of Alaska	NDBC	ARES	201	25.10.2012	VV
42058	74° 55'4'' W	14° 55'23'' N	Central Caribbean	NDBC	ARES 4.4	4161	27.10.2012	VV
42057	81° 30'2'' W	17° 0'8'' N	Western Caribbean	NDBC	ARES	462	31.10.2012	VV
42059	67° 28'19'' W	15° 3'14'' N	Eastern Caribbean	NDBC	ARES	4785	23.12.2012	VV
46002	130° 28'28'' W	42° 35'21'' N	West Oregon, US	NDBC	AMPS	3444	16.03.2013	VV

[6] Advanced Modular Payload System
[7] Automated Reporting Environmental System

5 METHOD

5.1 Deriving wavefield parameters from TerraSAR-X imagery

High-resolution products of TSX radar allow resolving of local fine-scale effects of wave fields. An algorithm to derive wave field parameters from SAR imagery was developed. Wave parameters were derived by implementing FFT analysis on SAR image amplitude spectra. Overview of the algorithm scheme can be seen in Appendix A. Overview of the algorithm to derive wave field parameters from TerraSAR-X imagery.

As a first step in the algorithm, output variables are to be declared. For the current work, following parameters were stored in the output file: wave propagation direction γ, wavenumber k and image energy density spectrum E.

Following the scheme, reading the digital numbers (DN) from image file for the further processing is done. As the entire image file is too capacious for reading at once, smaller subsamples are used. A value for subsample size is input by the user and the image is tiled accordingly. At the current work, subsample with dimensions 512x512 pixels (640x640 m) is used, resulting in continuous wave field image. An example of the subsample is seen in Figure 7a). If wave field is not variable in space and has similar wave characteristics for neighboring subsamples, it is possible to optimize the calculation by step over which the subsample reading is made.

In addition to image intensity, image metadata is needed for further processing. Information related to image projection, corner coordinates to calculate longitude and latitude fields, pixel spacing and number of columns and rows is acquired from image metadata. Local incidence angle of radar beam θ_i and image calibration coefficients k_s are needed for the radiometric calibration of SAR image.

Image calibration allows taking into account all the contributions in the radiometric values that are not due to the target characteristics. This permits to minimize the differences in the image radiometry and to make any TSX images obtained from different incidence angles, ascending-descending geometries and/or opposite look directions comparable. To give physically meaningful σ^0 values to the digital numbers, following equations are used:

$$\beta^0 = k_s * |DN|^2 \quad (7)$$

$$\beta_{DB}^0 = 10 \log_{10} \beta^0 \quad (8)$$

$$\sigma_{DB}^0 = \beta_{DB}^0 + 10 \log_{10} sin\theta_i \quad (9)$$

By implementing the calibration coefficient and incidence angle values, the DN values are converted to σ^0 values.

Retrieval of image spectrum and the related wave field parameters is a complex task, which consists of several sub-activities. Firstly, FFT operator is used to calculate image wavenumber spectrum. An example of calculated subsample is given in Figure 7b). The dominant wavelength, represented as maximum value on the spectrum image (Figure 7c)), and wave propagation direction can be read directly from the two dimensional spectrum using equations 4 and 5 respectively. Wave period is calculated according to equation 6. Total image energy density E is calculated from the SAR image wavenumber spectrum using the following equation:

$$E = \int_{k_{min}}^{k_{max}} \int_0^{2\pi} S(k, \varphi) dk d\varphi \quad (10)$$

where $S(k,\varphi)$ is image spectrum obtained through FFT. Wavenumber limits are set as following: k_{max} = 0.03 rad m^{-1} and k_{min} = 0.41 rad m^{-1} which corresponds to wavelengths L_{max} = 200 m and L_{min} = 15 m. Spectrum energy can be linked with significant wave height but remains beyond the scope of this paper.

After calculations, all parameters that were defined in the beginning are written into output file. Parameters that are located over land are blanked out.

For the current work, the results of SAR data processing are interpolated to SWAN wave model grid for easier comparison. The produced gridded satellite based

wave field products enable effective integration of remote sensing data into SWAN wave model for operational use.

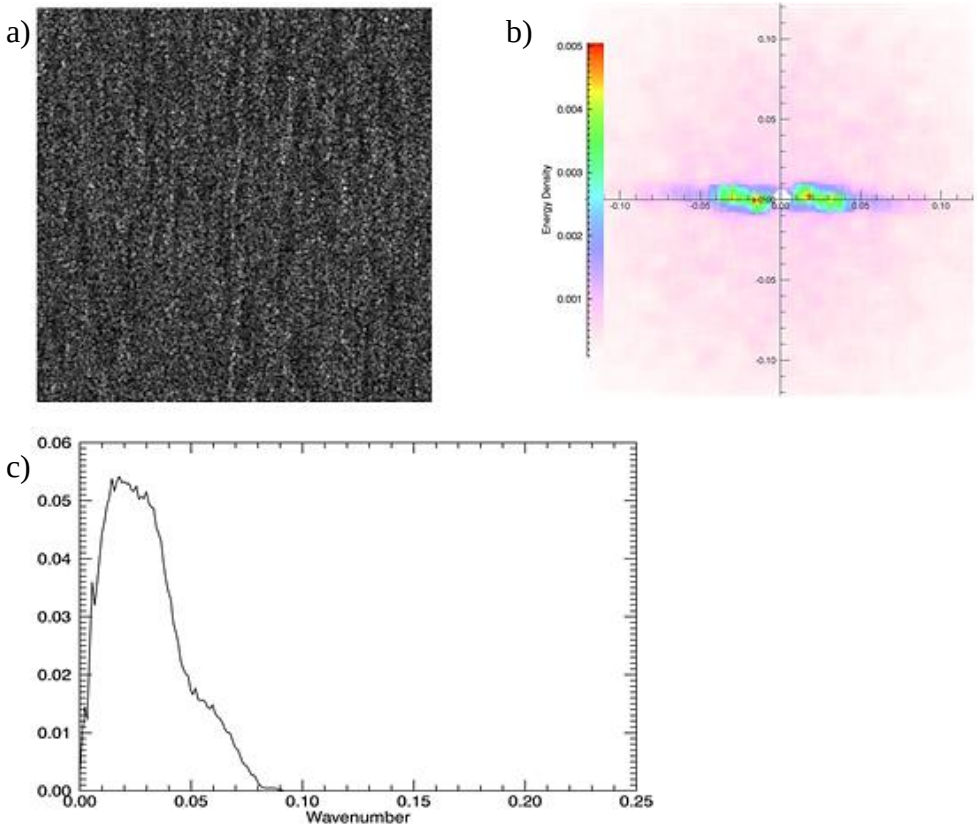

Figure 7. a) An example of selected subsample, b) calculated wavenumber spectrum from selected subsample using FFT operator and c) image wavenumber spectrum of the wave propagation direction.

5.2 Comparison of SAR results with buoy and wave model data

The results of wave field parameters derived from satellite imagery were compared with *in situ* measurements and wave model outputs. Wave propagation direction and peak periods from SAR calculations were collocated with wave model and *in situ* measurement values and presented on scatter plots with correlation coefficient *r*. Wave model allows to compare wavenumber using the same method mentioned above. Equation (6) allows the comparison of wave period. The root mean square deviation (RMSD) and bias were also calculated between SAR, *in situ* measurements and wave model values (SAR minus buoy or wave model values).

6 RESULTS

6.1 Validation of SAR results against buoy and wave model data

Figure 8 to Figure 10 show the comparison of derived TSX integrated sea state parameters collocated with *in situ* buoy measurements and SWAN wave model results. On the graphs, correlation coefficient *r*, number of observations (Nobs), root mean square deviation (RMSD) and systematic distortion from the average value (bias; SAR minus buoy or wave model results) is given.

Comparison demonstrates that TSX sensor is suitable for estimation of wave parameters in the Baltic Sea where the magnitude of wave characteristics (wavelength, period, wave height etc.) are significantly lower than in the open ocean. High correlation is seen in case of all the compared parameters. The results of the algorithm used show a correlation coefficient *r* of 0.95 for the peak direction of buoy versus SAR (RMSD = 30°; bias = 0.4°; Figure 8a)) and in case of wave model and SAR data comparison *r* was 0.87 (RMSD = 25°; bias = 0.16°; Figure 9a)). Peak wavelength from SAR data correlated well with buoy measurements and model results, with the corresponding *r* values of 0.81 (RMSD = 13.2 m; bias = -0.18 m; Figure 8b)) and 0.89 (RMSD = 9.4 m; bias = -0.006 m; Figure 9b)).

Peak period calculated from SAR 2D spectrum showed slightly lower correlation coefficients. The correlation coefficient between measured peak wave period and SAR based peak wave period was 0.68 (RMSD = 1.38 s; bias = 0.02 s; Figure 10a)) and in case of wave model and SAR data comparison the *r* was 0.62 (RMSD = 1.19 s; bias = 0.005 s; Figure 10b)). Summary of statistical parameters can be seen in Appendix B. Statistical characteristics between wave parameters (direction, wavelength and period).

Peak period results from SAR imagery show values corresponding to the Leppäranta & Myrberg (2009), rarely exceeding 7 - 8 s. Peak periods from Figure 10a) and Figure 10b) remain mainly between 3 - 8 s which coincides earlier results.

Experiments showed no correlation between measured average period and calculated average period from TSX spectrum. Some of the data of wave measurements is received from foreign source (Table 2) and due to lack of knowledge about the exact algorithm used in data management processes, average periods were not compared.

Peak wavelengths and peak periods should show similar statistical values as the results are connected to each other with the dispersion relationship (equation 6). The difference seen in Figure 10a) and Figure 10b) might come because of the different topography settings.

The SAR data was collected using different polarizations in order to assess the SAR wave retrieval algorithm dependence on polarization (Figure 8 to Figure 10). It was demonstrated that the developed algorithm is independent of polarization, imaging mode and location thus it is universally applicable on different images to retrieve wave field parameters (wavelength, wave direction and period).

It is due to the location of the Baltic Sea in temperate latitudes that wave propagation directions are rather homogeneous (Figure 8a) and Figure 9a)). As described in Section 2.1 wind blows dominantly from sector 180-270° (S, SW, W). Moreover, waves in the GoF tend to propagate along the longer axis of the gulf which furthermore explains the similarity.

Dominant wavelengths are brought out in Kriaučiūnienė et al. (2006). They suggested that wavelengths mainly remain between 20 - 70 m and during storm can reach up to 130 m. Although, our images were acquired during higher winds, wavelengths (Figure 8b) and Figure 9b)) show similar values, mainly between 20 - 80 m.

Our results show that TSX sensor is capable to detect even shorter waves than earlier suggested 30 m (Lehner, et al., 2012). On Figure 8b) and Figure 9b) the lower limit of the wavelength is around 20 m.

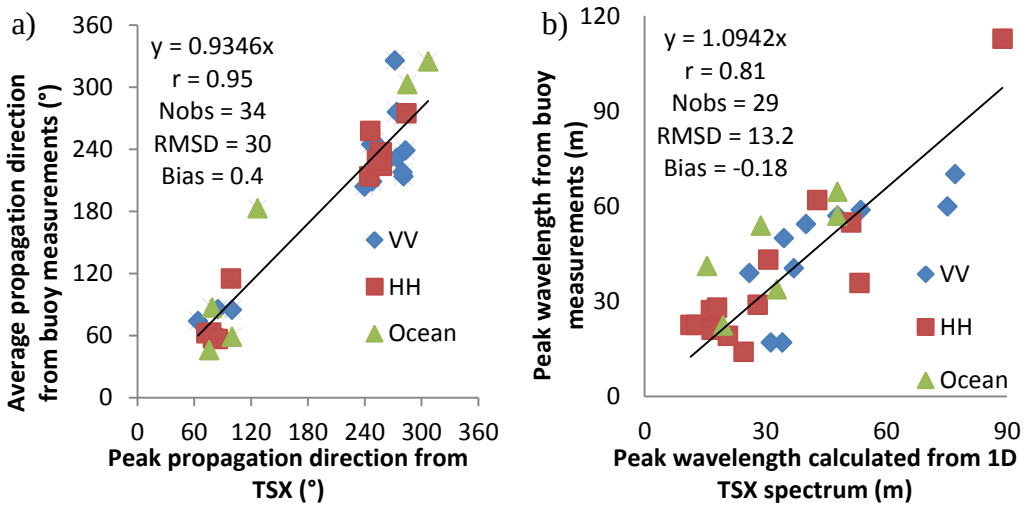

Figure 8. a) Wave propagation direction derived from TSX compared to *in situ* measurements, b) Peak wavelength calculated from TSX spectrum data compared to wavelengths calculated from peak period of buoy measurements using equation 6.

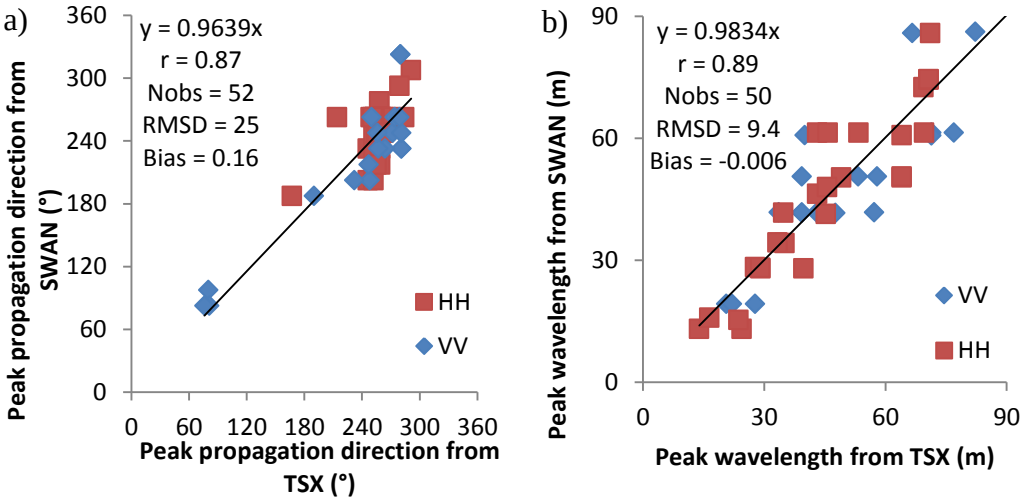

Figure 9. a) Wave propagation direction derived from TSX compared to SWAN wave model results, b) Peak wavelength retrieved from TSX spectrum compared to peak wavelengths from SWAN.

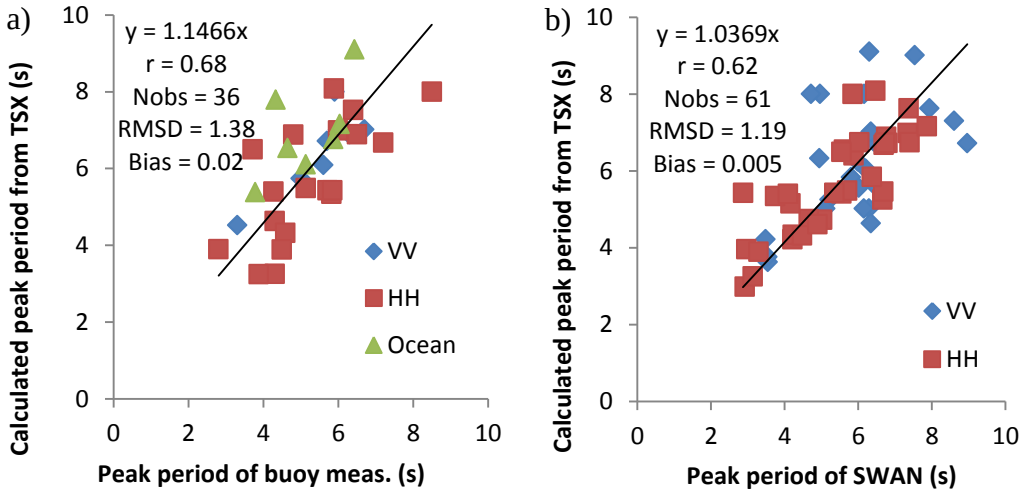

Figure 10. a) Wave peak period from buoy measurements compared to calculated results from TSX data, b) Wave peak period from SWAN wavemodel collocated to results from TSX.

6.2 Case study over Tallinn Bay area

We present a case showing a TSX data comparison with an *in situ* measured wave spectrum. TSX Stripmap image with VV polarization was acquired over Tallinn Bay area in the Gulf of Finland (Figure 1) on 29 October, 2013 15:45 UTC (Figure 11a)). In this case, there was a temporary buoy which provided wave frequency spectrum. The 1D spectrum derived from TSX and the one given by buoy show good agreement, as can be seen in Figure 12c). Corresponding sub-scene and 2D spectrum is given in Figure 12a) and Figure 12b). There is a slight shift in the peaks on the 1D spectrum which might be due to backscattering noise of the radar image.

Sea state characteristics in coastal areas change rapidly in the spatial domain (Li, et al., 2010; Lehner, et al., 2012; Brusch, et al., 2011) and SAR imagery provides an opportunity to indirectly measure wave field parameters with high spatial resolution. It must be emphasized that in the Baltic Sea, well developed and structural sea state is required to retrieve proper spectrum and hence correct wave properties.

In the following example, we examined wave field parameters in three different locations (Figure 11a)). In the middle of the Gulf of Finland (Figure 13a)) the waves are propagating in the direction of the wind from W-SW and the corresponding wave

propagation direction derived from SAR 2D wavenumber spectrum is 86˚. On the sub-images near the island of Naissaare (Figure 13b) and c)) demonstrate land shadow effect. As waves are propagating from W-SW, it is clear, that waves are refracted by the island. Figure 13b) represents the sub-scene northwest from the island of Naissaare. Wave propagation direction is 120° whereas on the sub-scene extracted from southern part of the Naissaare coast (Figure 13c)) the peak wave propagation direction is 60°. The wavelengths of refracted waves are similar (Figure 14). However, the refracted wave fields (Figure 14b) and c)) are more heterogeneous (variable wave lengths and wave directions) compared to the wave field in the central part of the Gulf of Finland (Figure 14a)). Dissolution is on the one side caused by refraction but might also be caused by bottom topography.

We can somewhat observe wavelength decrease near the coastal areas, where bottom topography (Figure 11c)) starts to dissolve wavelengths. This phenomonon can be noticed on waves that are propagating into Tallinn Bay from below of the Naissaare island.

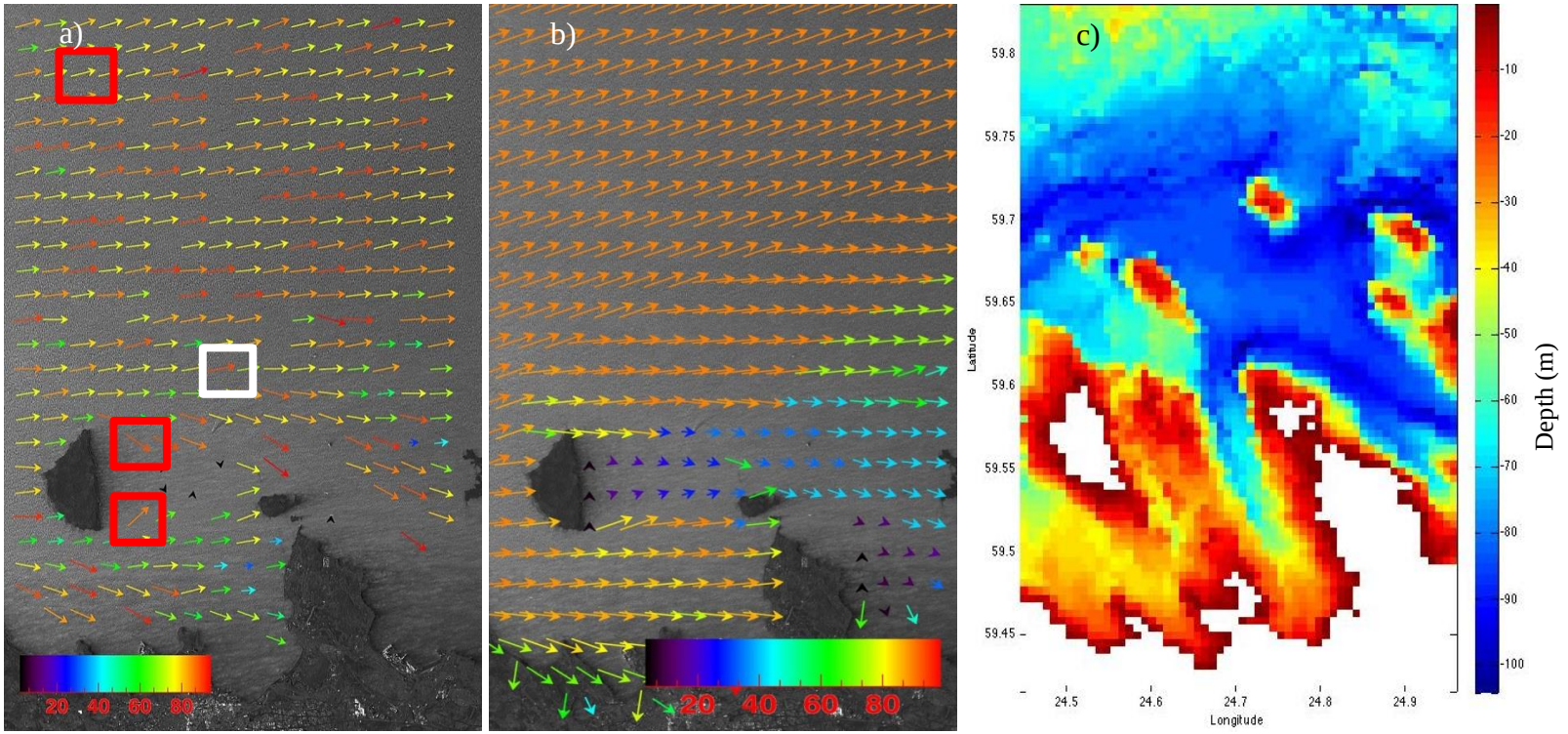

Figure 11. a) Wavelength field derived from TSX Stripmap image, VV polarized, acquired 29 October, 2013 15:45 UTC. The white box is the location of the buoy and the red boxes are the cases presented in Figure 13 and Figure 14, b) Wavelength field calculated by SWAN wave model, c) Bottom topography over the location (Baltic Sea Hydrographic Commission, 2013).

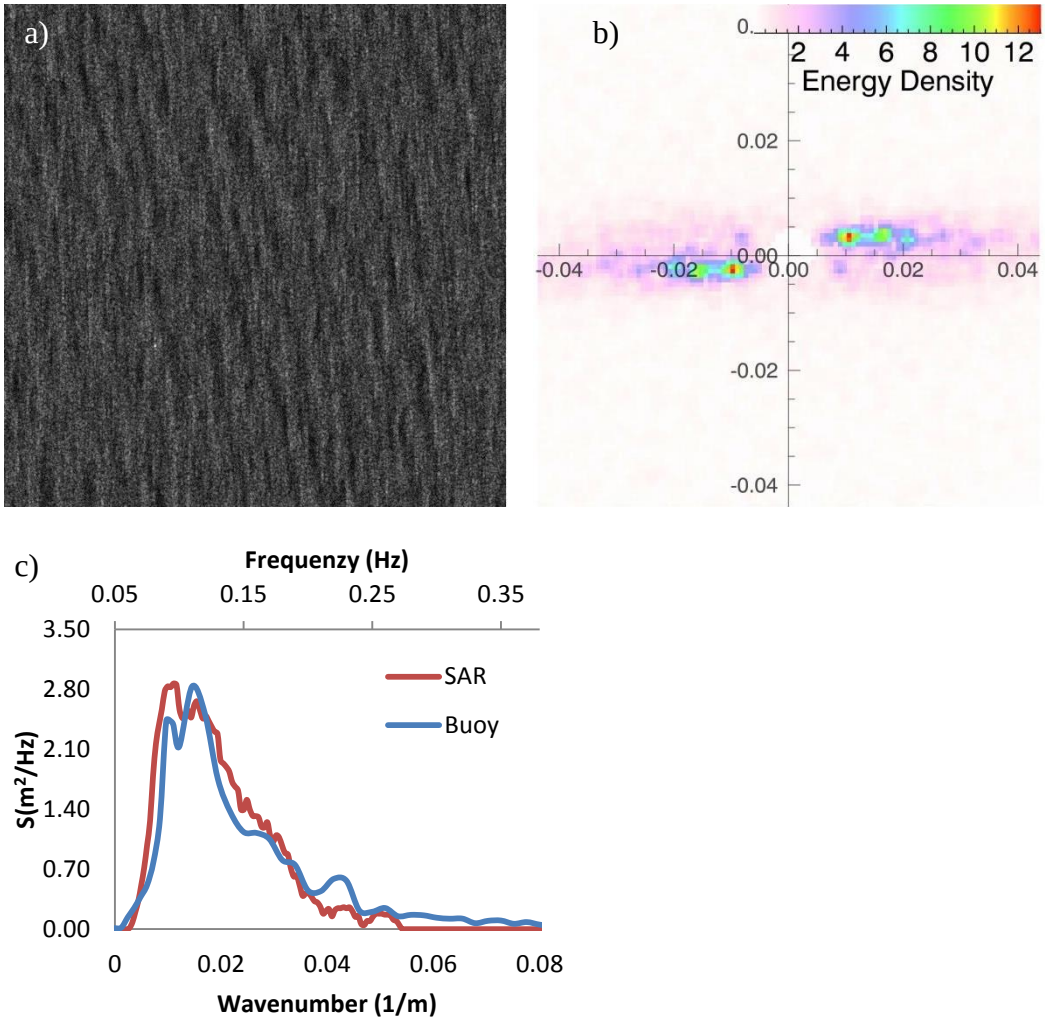

Figure 12. a) TSX 512x512 pixels VV polarized sub-scene taken over buoy station presented in Figure 11a) (white box), b) 2D SAR wavenumber spectrum, c) 1D spectrum.

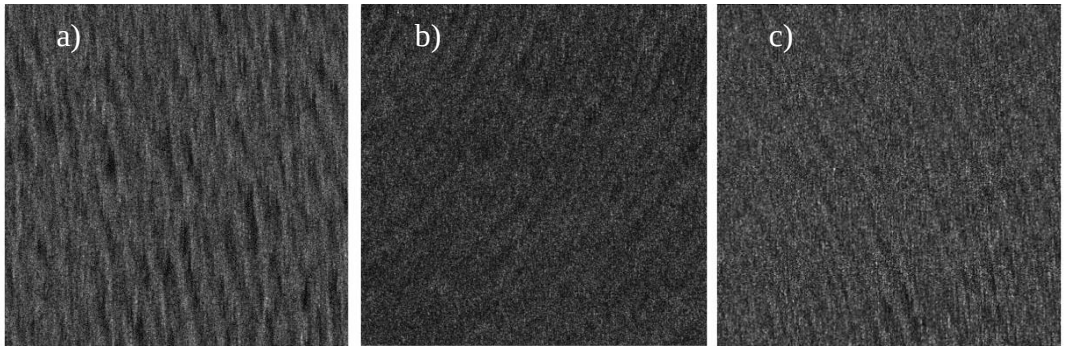

Figure 13. TSX 512x512 pixels sub-scenes from VV polarized image acquired 29 October, 2013 15:45 UTC, a) is the box in the top of TSX wave field in Figure 11a), b) is the box in the middle and c) is the box in the bottom.

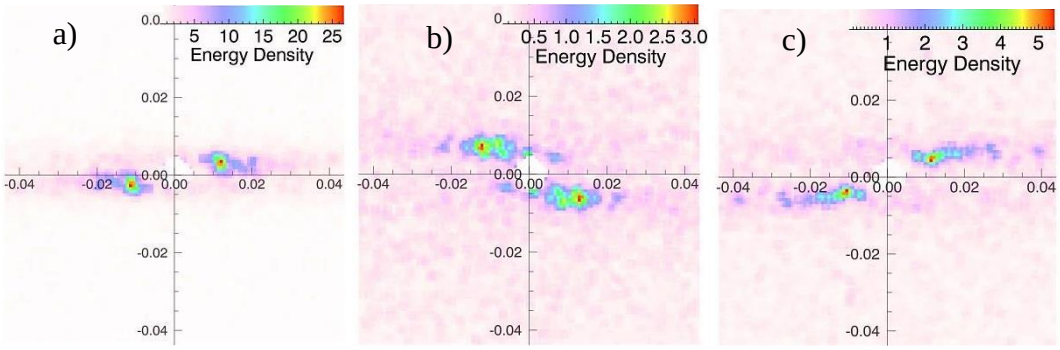

Figure 14. 2D wavenumber spectrums derived from TSX sub-scenes presented on Figure 13. In a) the wave propagation direction is 86°, in b) it is 120° and in c) direction is 60°. Wavelengths are 82 m, 80 m, and 84 m correspondingly.

6.3 Comparison with wave model using case studies

In the current section, we are looking the operational usage of TSX products. For the ocean, spatial coverage of the Stripmap image is not sufficient enough to be used as operational products for wave model assimilation, although it can be used for model validation. In the Baltic Sea on the other hand, operational use could be set up. Acknowledgement of high correlation coefficients between wave propagation directions (Figure 8a)), wavelengths (Figure 8b)) and also peak period (Figure 10a)), is a good reason to test how wave model results could be improved by detailed information from SAR imagery.

We are looking two case studies, one acquainted in previous section (Figure 11a)) and another from 16 September, 2012 16:02 UTC. Wave field parameters (wave propagation direction and wavelength) on SAR image are interpolated to SWAN wave model one nautical mile grid and standard deviation is analyzed.

Both cases show that SAR data is more variable than wave model. For the first case standard deviation of wave propagation direction is 21.9° for SWAN and 26.8° for SAR and for the wavelength 8.4 m and 9.6 m correspondingly. The second case show similar outcome. Here the variability difference is even larger, for the wave propagation direction the standard deviation for SWAN is 12.7° and for the SAR it is 23.4°. The same is seen in wavelength values, for SWAN 9.3 m and for SAR 20.7 m.

Two case studies demonstrate that observed wave fields (SAR) are more complex than it is often pictured with the wave model forecasts. This is especially well seen around islands where waves are refracted. Thus, information retrieved from SAR imagery can strongly improve wave model outcomes.

One example of low variability wavelength field can be seen in Figure 11b). The same Tallinn Bay area as described in Section 6.2 is used. Although, the wavelengths and wave propagation directions are similar to SAR results (Figure 11a)), variability is significantly lower.

The largest difference can be seen from East of the Viimsi peninsula. Results from SAR imagery show that waves continue to propagate into the Muuga bay with similar wavelengths as in open part of the GoF whereas results from wave model show significant decrease in wavelengths. From the topography field (Figure 11c)) we can conclude that theoretically waves as long as retrieved from SAR imagery are possible over current location.

6.4 Testing the developed method over open ocean

With our Baltic Sea dataset, we have not been able to investigate some complex wave fields (swell and wind wave interaction), therefore we examined images from open ocean. Although there are a great deal of locations in the Baltic Sea where waves can interact to each other and cause difficult wave fields, the scale of the diffracted waves are below the radar detection limit. Therefore, during the following section, spectrums with several peaks are observed over the open ocean.

On TSX image acquired 25 October, 2012 03:15 UTC (Figure 15a)) rather complex wave field is presented. On the two-dimensional spectrum (Figure 17a)) two wave systems with different wavelengths can be visualized. There are two dominant peak wavelengths, longer wavelengths around 60 m and shorter around 30 m. This result is confirmed by one-dimensional spectrum (Figure 18a)), where good agreement between TSX wavenumber spectrum and buoy frequency spectrum is seen.

Another complex wave field case can be observed on Figure 15b) which is rather classical case on large water bodies. Long swell waves interact with shorter ones generated by the local wind regime causing complicated situations for navigators.

On 2D spectrum (Figure 17b)), two dominant wavelengths with different propagation direction is seen. Longer waves, around 120 m where propagating to South-East, whereas shorter waves with wavelengths about 60 m where propagating nearly to the East (Figure 17b)). From 1D spectrum (Figure 18b)) we can confirm that shorter waves had more energy but longer swell waves had also a significant contribution (upper part of Figure 15b)).

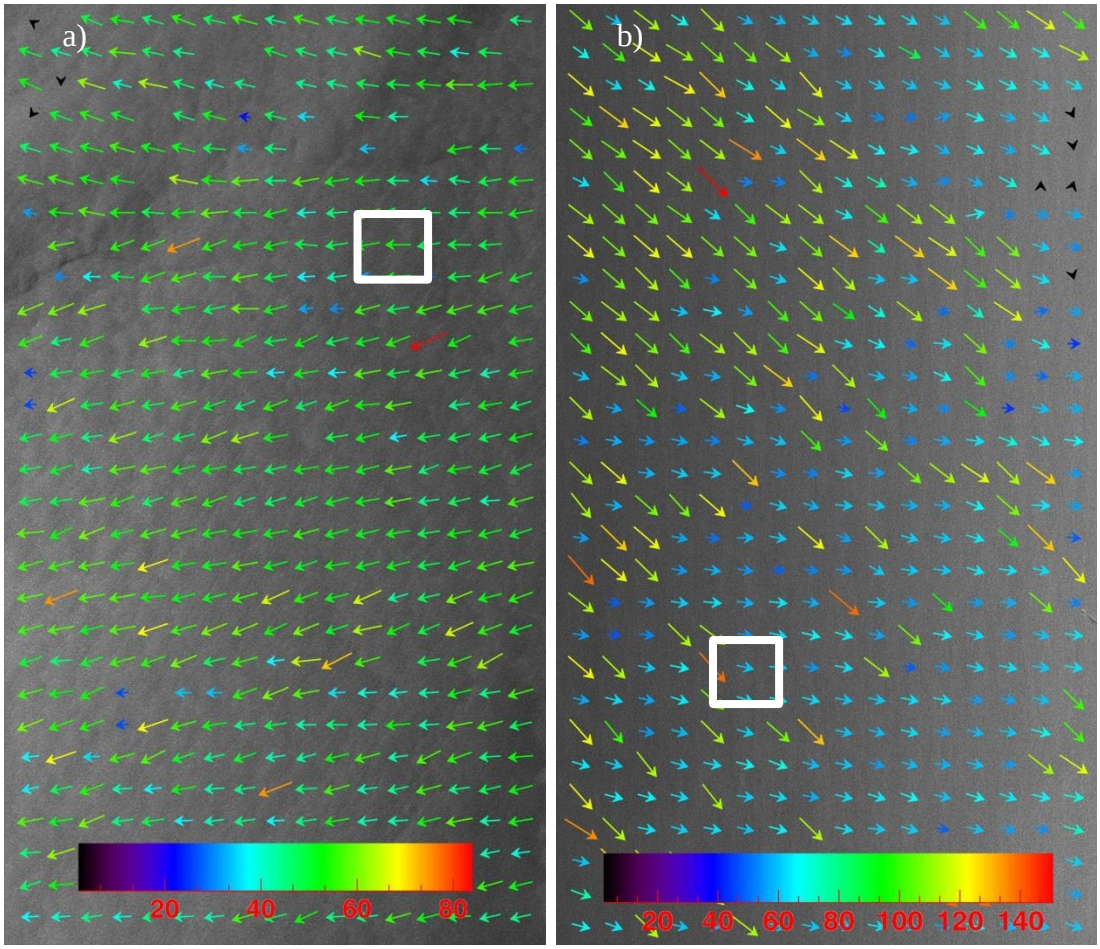

Figure 15. Wavelength field derived from TSX Stripmap image, a) acquired 25 October, 2012 03:15 UTC, VV polarized, buoy 46076 (Table 3), b) acquired 31 October, 2012 11:28 UTC, VV polarized, buoy 42057 (Table 3). White boxes are the location of the buoys correspondingly.

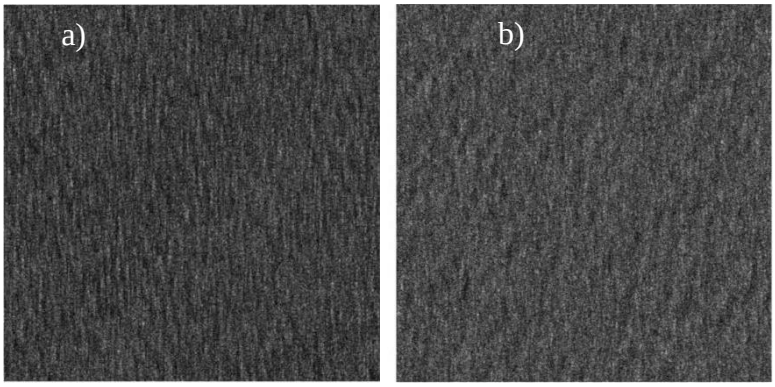

Figure 16. a) TSX 512x512 pixels sub-scene acquired 25 October, 2012 03:15 UTC, VV polarized, buoy 46076, b) TSX 512x512 pixels sub-scene acquired 31 October, 2012 11:28 UTC, VV polarized, buoy 42057.

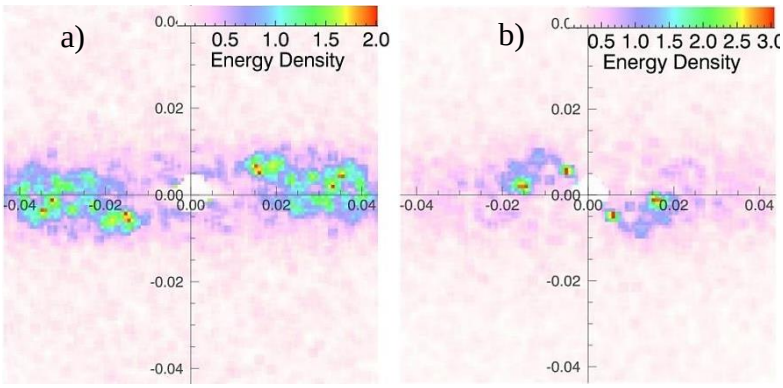

Figure 17. a) 2D wavenumber spectrums derived from TSX sub-scenes, 25 October, 2012 03:15 UTC and b) 2D wavenumber spectrums derived from TSX sub-scenes, 31 October, 2012 11:28 UTC.

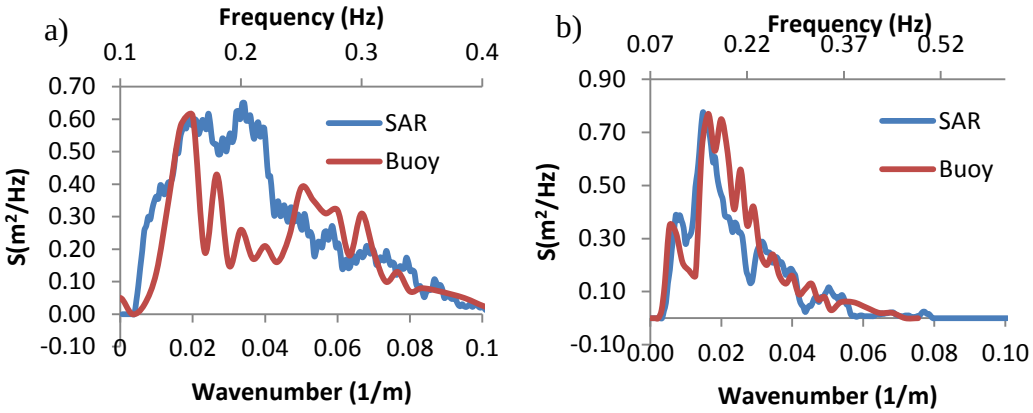

Figure 18. a) 1D wavenumber spectrums derived from TSX 2D spectrums compared to frequency spectrum, 25 October, 2012 03:15 UTC, b) 1D wavenumber spectrums derived from TSX 2D spectrums compared to frequency spectrum, 31 October, 2012 11:28 UTC.

7 CONCLUSION

X-band SAR sensor has proven its usability over the Baltic Sea region. It is shown, that significantly lower wavefield parameters compared to open ocean are detectable by the sensor. It can be said, that radar mechanisms (tilt, hydrodynamic and velocity bunching modulation) for detecting waves work good on the scale of the Baltic Sea. Unfortunately we have not been able to analyse waves that are propagating along the satellite path. This is mainly due to the location of the Baltic Sea in the temperate latitudes, where winds from S, SW and W are dominant which coincides with the range direction of SAR sensor. Wavelengths in the Baltic Sea are mainly distributed between 20 to 70 m and for the stormy case up to 130 m which is the cause of the selection of wavelenght limits.

A method was developed for detection of wave field parameters (direction, wavelength, period) from SAR imagery in the Balti Sea. It was found out that TSX sensor is capable to detect wavelength values of 20 m. The upper limit of detectable wavelength was set to 200 m. Well developed wavefields are required in order to retrieve proper spectrum and hence correct wavefield parameters from SAR imagery. Therefore TSX images are acquired during the time of rather strong winds, mainly in the autumn of 2013.

Comparison of SAR data with buoy measurements and wave model outputs showed good correlation between all compared parameters. Significant correlation is seen between SAR derived and buoy measured wave propagation direction (r = 0.95, RMSD = 30°, bias = 0.4°) and wavelengths (r = 0.81, RMSD = 13.2 m, bias -0.18 m). Comparison of SAR based wave field information with SWAN wave model outputs showed also good agreement in case of wave propagation direction (r = 0.87, RMSD = 25°, bias = 0.16°) and wavelengths (r = 0.89, RMSD = 9.4 m, bias = -0.006 m).

Peak period calculated from SAR 2D spectrum showed slightly lower correlation coefficients: (i) buoy versus SAR the *r* was 0.68 (RMSD = 1.38 s; bias = 0.02 s) and (ii) wavemodel versus SAR *r* of 0.62 (RMSD = 1.19 s; bias = 0.005 s).

Exaples of image spectra with several peaks are also presented in the study. It was demonstrated that SAR image spectra correspond well with the measured spectral wave density.

The results of wavefield parameters received with the algorithm did not depend on the location nor the imaging mode nor the polarization. Therefore, it can be concluded that the algorithm is applicable also outside of the Baltic Sea.

It was demonstrated that SAR images enable to evaluate small scale wave field variations in the coastal zones where sea state characteristics change rapidly in the spatial domain. Case study showed that SAR sensor enables to track refracted waves around shallow areas with islands and peninsulas. Dissolution of the waves due to refraction and bottom topography is aslo seen in regions sheltered by by island (2D spectrum is more heterogeneous when compared with spectrum of central part of the bay).

High resolution satellite images with detailed wave information give a good opportunity for integrating wave model and remote sensing data. Analysis showed that information from SAR imagery is more variable than wave model outputs.

ABSTRACT

Current study is focused on detection of wave field parameters from SAR imagery in the Baltic Sea. Study is carried out over the Baltic Sea region where common SW and W winds induce steep waves with shorter wavelengths compared to ocean waves. As TerraSAR-X data has high spatial resolution (0.75 – 1.5m per pixel) compared to previous SAR sensors (e.g. ENVISAT/ASAR), it enables to detect the two-dimensional wave spectrum even in the Baltic Sea.

Main objective of this work was to demonstrate the capability of detecting wave field parameter from TerraSAR-X imagery in the Baltic Sea. The wave field parameters obtained from SAR imagery were compared with in situ measurements and SWAN wave model.

The comparison showed significant correlation between SWAN and SAR derived wave propagation direction (r = 0.87; RMSD = 25˚) and wavelengths (r = 0.89; RMSD = 9.4 m). Peak period was also calculated from SAR based 2D wavenumber spectrum and compared with SWAN results (r = 0.62; RMSD = 1.19 s). Comparison of SAR based wave field information with buoy measurements showed also good agreement in case of wave propagation direction (r = 0.95 and RMSD = 30˚), wavelengths (r = 0.81; RMSD = 13.2 m) and peak period (r = 0.68; RMSD = 1.38 s).

Case studies showed that SAR data enables to detect land shadow effects and small scale wave field variations in the coastal zone. It was shown that SAR data (which shows large spatial variability) is also valuable for improving and interpreting wave model results (smaller spatial variability).

RESÜMEE

Käesolev töö on fokusseeritud radari kasutusvõimalustele Läänemere piirkonnas. Uurimispiirkonnas domineerivad läänetuuled tekitavad laineid, mis on võrreldes ookeanilainetega lühikesed ja järsud. Varasemate radarsensorite abil pole olnud võimalik tuvastada Läänemere lained sellise detailsusega nagu seda lubab teha TerraSAR-X sensor. Selle kõrglahutuslikud andmed võimaldavad leida kahedimensionaalset pildispektrit isegi kitsastes lahtedes Läänemere piirkonnas.

Töö põhieesmärk on demonstreerida TerraSAR-X sensori võimekust hoopis väiksemas skaalas, kui seda seni tehtud on. Laineparameetrite väärtused SAR andmetelt on võrreldud *in situ* mõõtmistega ja SWAN lainemudeli andmetega.

Võrreldud parameetrid, laine levimise suund, lainepikkus ja piigi periood, korreleerusid omavahel hästi. SWAN'i ja SAR'i tulemuste vaheline võrdlus näitas kõrget korrelatsiooni laine levimise suundade (r = 0.87; RMSD = 25˚), lainepikkuste (r = 0.89; RMSD = 9.4 m) ja piigi perioodide vahel (r = 0.62; RMSD = 1.19 s). Tulemuste võrdlus poi andmetega näitas samuti head kokkulangevust laine levimise suuna (r = 0.95; RMSD = 30˚), lainepikkuse (r = 0.81; RMSD = 13.2 m) ja piigi perioodi (r = 0.68; RMSD = 1.38 s) korral.

Juhtumiuuringud näitasid SAR sensori kasulikkust just saarelähedastel aladel, kus esinevad ruumis muutlikud laineväljad. Sel põhjusel testiti ka SAR andmete kasutamist lainemudel prognooside parendamisel.

REFERENCES

Alari, V. 2013. *Multi-Scale Wind Wave Modeling in the Baltic Sea*. PhD dissertation, Tallinn University of Technology.

Alari, V. and Kõuts, T. 2012. Simulating wave-surge interaction in a non-tidal bay during cyclone Gudrun in January 2005. *Baltic International Symposium (BALTIC), 2012 IEEE/OES*: 1-12.

Baltic Sea Hydrographic Commission. 2013. *Baltic Sea Bathymetry Database*. http://data.bshc.pro (Accessed 25.03.2014).

Beal, R. C., Tilley, D. G. and Monaldo, F. M. 1983. Large- and small-scale spatial evolution of digitally processed ocean surface wave spectra from the SEASAT synthetic aperture radar. *Journal of GeoPhysical Research: Oceans (1978-2012)* 88: 1761-1778.

Bruck, M. and Lehner, S. 2013. Coastal wave field extraction using TerraSAR-X data. *Journal of Applied Remote Sensing* 7.

Brusch, S., Held, P., Lehner, S., Rosenthal, W. and Pleskachevsky, A. 2011. Underwater bottom topography in the coastal areas from TerraSAR-X data. *International Journal of Remote Sensing* 32: 4527-4543.

Diaz Méndez, G. M., Lehner, S., Ocampo-Torres, F. J., Ming Li, X. and Brusch, S. 2010. Wind and wave observations off the south Pacific Coast of Mexico using TerraSAR-X imagery. *International Journal of Remote Sensing* 31: 4933-4955.

Eineder, M., Fritz, T., Mittermayer, J., Roth, A., Boerner, E. and Breit, H. 2008. *TerraSAR-X Ground Segment, Basic Product Specification Document*. No. TX-GS-DD-3302. CLUSTER APPLIED REMOTE SENSING (CAF) OBERPFAFFENHOFEN (GERMANY).

Jaagus, J. and Kull, A. 2011. Changes in surface wind direction in Estonia during 1966-2008 and their relationships with large-scale atmospheric circulation. *Estonian Journal of Earth Sciences* 60: 220-231.

Jackson, C. H. and Koch, W. 2005. Synthetic aperture radar marine user's manual. www.sarusermanual.com (Accessed 11.03.2014).

Kahma, K. K. 1976. Preliminary results of wind wave measurements in the southern part of the Bothnian Sea. In: *Proceedings of the 10th conference of the Baltic Oceanographers*, Part 1, Göteborg, Sweden.

Kahma, K. K. 1981. A study of the growth of the wave spectrum with fetch. *Journal of Physical Oceanography* 11: 1503-1515.

Kahma, K. K. and Petterson, H. 1993. Wave statistics from the Gulf of Finland. *Finnish Institute of Marine Report*.

Kahma, K. K., Pettersson, H. and Tuomi, L. 2003. Scatter diagram wave statistics from the northern Baltic Sea. *MERI – Report Series of the Finnish Institute of Marine Research* 49: 15-32.

Komen, G. J., Cavaleri, L., Donelan, M., Hasselmann, K., Hasselmann, S. and Janssen, P.A.E.M. 1996. *Dynamics and modelling of ocean waves*. Cambridge University Press.

Kriaučiūnienė, J., Gailiušis, B. and Kovalenkovienė, M. 2006. Peculiarities of sea wave propagation in Klaipeda Strait, Lithuania. *BALTICA* 19: 20-29.

Lehner, S., Horstmann, J., Koch, J. and Rosenthal, W. 1998. Mesoscale wind measurements using recalibrated ERS SAR images. *Journal of Geophysical Research: Oceans (1978-2012)* 103: 7847-7856.

Lehner, S., Schulz-Stellenfleth, J., Brusch, S. and Ming Li, X. 2008. Use of TerraSAR-X Data for Oceanography. In *Synthetic Aperture Radar (EUSAR), 2008 7th European Conference*.

Lehner, S., Pleskachevsky, A. and Bruck, M. 2012. High-resolution satellite measurements of coastal wind field and sea state. *International Journal of Remote Sensing* 33: 7337-7360.

Leppäranta, M. and Myrberg, K. 2009. *Physical oceanography of the Baltic Sea*. Springer Praxis.

Ming Li, X., Lehner, S. and Wolfgang, R. 2010. Investigation of Ocean Surface Wave Refraction using TerraSAR-X Data. *IEEE Transactions on Geoscience and Remote Sensing* 48: 830-840.

Pettersson, H., Kimmo, K. K. and Tuomi, L. 2010. Wave Directions in a Narrow Bay. *Journal of Physical Oceanography* 40.

Raudsepp, U., Laanemets, J., Haran, G., Alari, V., Pavelson, J. and Kõuts, T. 2011. Flow, waves, and water exchange in the Suur Strait, Gulf of Riga, in 2008. *Oceanologia* 53: 35-56.

Räämet, A. 2010. *Spatio-Temporal Variability of the Baltic Sea Wave Fields*. PhD dissertation, Tallinn University of Technology.

Soomere, T., Behrens, A., Tuomi, L. and Nielsen, J. W. 2008. Wave conditions in the Baltic Proper and in the Gulf of Finland during windstorm Gudrun. *Natural Hazards and Earth System Sciences* 8: 37-46.

Suursaar, Ü., Kullas, T. and Aps, R. 2012. Currents and waves in the northern Gulf of Riga: measurements and long-term hindcast. *Oceanologia* 54: 421-447.

SWAN team. 2014. http://swanmodel.sourceforge.net/ (Accessed 15.04.2014).

The WAMDI Group. 1988. The WAM model - A Third Generation Ocean Wave Prediction Model. *Journal of Physical Oceanography* 18: 1775-1810.

Tuomi, L., Kahma, K. K. and Pettersson, H. 2011. Wave hindcast statistics in the seosonally ice-covered Baltic Sea. *Boreal Environment Research* 16: 451-472.

Voormansik, K. 2014. *X-band Synthetic aperture radar applications for environmental monitoring*. PhD dissertation, University of Tartu.

APPENDIXES

Appendix A. Overview of the algorithm to derive wave field parameters from TerraSAR-X imagery.

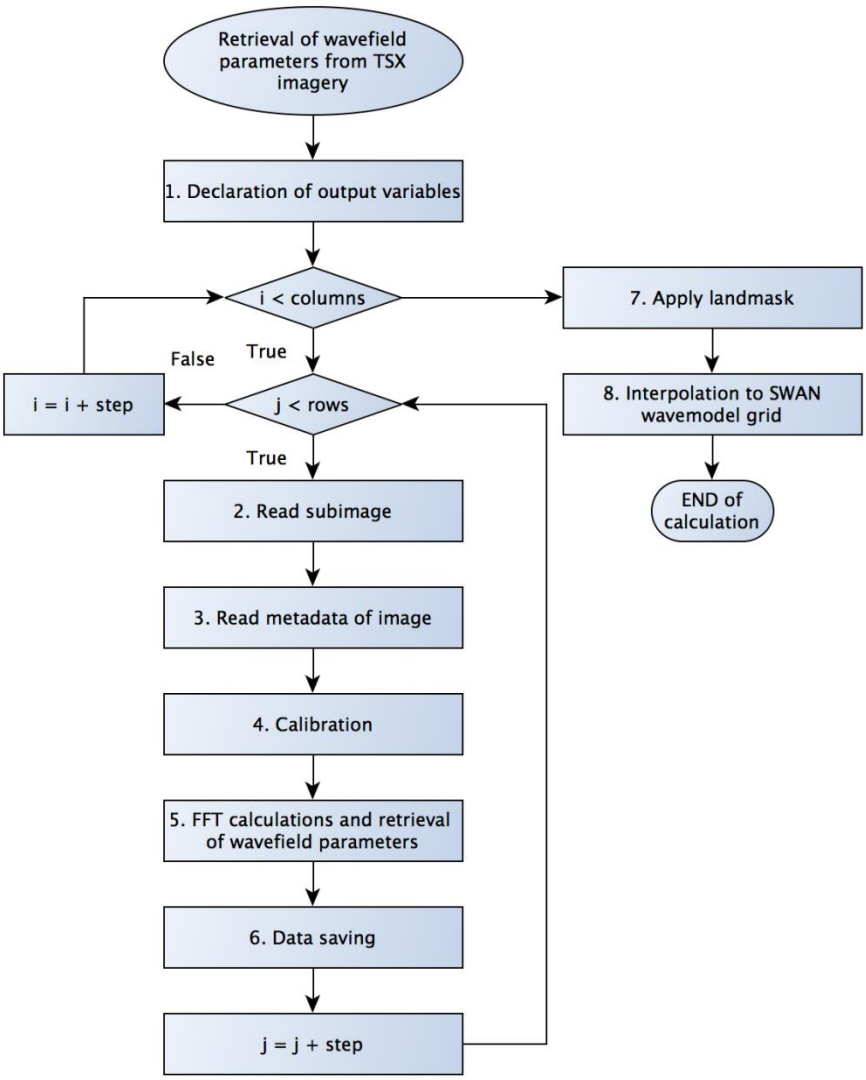

Figure. Algorithm to retrieve desired wave field parameters from TSX image. Possible to calculate parameters to every pixel – depending on the step.

Appendix B. Statistical characteristics between wave parameters (direction, wavelength and period)

	r	RMSD	Bias	Nobs	y
Buoy vs SAR					
Direction (°)	0.95	30	0.4	34	0.93
Wavelength (m)	0.81	13.2	-0.18	29	1.09
Peak period (s)	0.68	1.38	0.02	36	1.15
SWAN vs SAR					
Direction (°)	0.87	25	0.16	52	0.96
Wavelength (m)	0.89	9.4	0.006	50	0.98
Peak period (s)	0.62	1.19	0.005	61	1.04